

Chapter 5

Analysis and Results

Since the data analysis was very similar for both experiments, it will be described in the following only for the measurement performed at IUAC.

5.1 Data Analysis with INGASORT

The standard **INGASORT** analysis package [36] was modified to incorporate the additional signals obtained from the Coulomb excitation experiment. The command **PPAC** gave information about the ϕ -angles (ranging from 1-20) depending on which PPAC TAC was non-zero and also identified the multi-hit events. Multi-hit events (cross talk between neighbouring ϕ -segments) were less than 5% of the total events. In the IUAC experiment only one reaction partner could be measured at a given time, either the scattered projectile or the recoil nucleus (see Chapter 4.2). The existing **TDC** command could identify which pair of delay line signals had data and determined the difference between them. **CLOVER** command was used to match amplifier gains and provided the add-back energies of the Clover detectors. In addition, it identified which of the segments had data allowing for segment-wise Doppler correction. The Doppler correction was incorporated in the **USER** command that used the information from the Clover angles ($\vartheta_\gamma, \varphi_\gamma$) and the PPAC signals (ϑ_p, φ_p) computed from input data.

5.2 Add-back of the Individual γ -Ray Signals within a Clover Ge-Detector

In both experiments γ -ray detectors were used which consisted of four Ge-crystals arranged like a clover leaf. As mentioned before, their γ -ray energies were readout individually. Since the Ge-crystals are closely packed within a Clover detector, the Compton scattered γ -rays usually escaping a single Ge-crystal might be registered by the surrounding three Ge-crystals. In this way these γ -ray signals, which usually form the Compton background, add up to the

photopeak of the γ -ray transition.

Crystal No	COUNTS	
	^{112}Sn excitation	^{58}Ni excitation
1	11367 \pm 319	4661 \pm 171
2	12786 \pm 293	5151 \pm 137
3	10893 \pm 292	4391 \pm 149
4	10045 \pm 297	3998 \pm 161
SUM	45091 \pm 601	18201 \pm 310
ADD BACK	68013 \pm 721	27681 \pm 397

Table 5.1: Add-back ratio for Clover-3 used in the IUAC experiment

From the energy data of individual crystals, the gain in photopeak efficiency, the so-called add-back factor, could be determined (using INGASORT command *area* or *fit*). For Clover-3 the add-back factor for the $2^+ \rightarrow 0^+$ transition in ^{112}Sn and ^{58}Ni (see Table. 5.1) was determined to be ~ 1.5 calculated by the ratio of counts in the add-back spectrum relative to the sum of the counts in the individual Ge-spectra. In order to reduce the uncertainties, the analysis was performed for the Doppler-corrected peaks.

5.3 Particle Identification at IUAC

Fig. 4.5 shows the calculated kinetic energies of the ^{58}Ni projectiles and ^{112}Sn recoils based on two-body kinematics for the angular range 15° to 45° (dashed lines). Due to the use of rather thick entrance window ($10\mu\text{m}$ MYLAR, $\rho=1.39\text{ g/cm}^3$) for the PPAC, the detected kinetic energies of the ^{58}Ni projectiles and ^{112}Sn recoils were much lower (full drawn lines). The energy loss in MYLAR was taken from Northcliff and Schilling [32]. In the following it will be shown that the fast anode signals in the PPAC for both particles were sufficiently large to trigger the timing electronics. The corresponding slower cathode signal for the recoiling ^{112}Sn nuclei, which was used for the delay-line read out of the angle ($\sim \tan\theta$) information, was however below the detection threshold. In this way the close collision ($\theta_{cm}=90^\circ$ - 150°) events were not considered in the present measurement.

Fig. 5.1 shows the ungated γ -ray energy spectrum, coloured in black, measured with one of the Clover detectors in coincidence with PPAC detector. Six broad peaks, three each in the vicinity of 1.2 MeV and 1.4 MeV, could be identified. From kinematics (see Tab. 5.2), they can be identified as projectile excitation (~ 1.4 MeV) and target excitation (~ 1.2 MeV) for values ϕ_{12} ranging between 0° and 180° where $\phi_{12} = |\phi_\gamma - \phi_p|$. From phase space consideration one expects to see peaks at $E_\gamma = 1200\text{keV}$, 1233keV and 1264keV corresponding to ^{112}Sn and at $E_\gamma=1350\text{keV}$, 1413keV and 1495keV corresponding to ^{58}Ni excitation.

PPAC signal	ϕ_{12}	^{58}Ni excitation	^{112}Sn excitation
Nickel detected	0	1413	1233
	90	1381	1249
	180	1350	1264
Sn detected	0	1410	1235
	90	1451	1217
	180	1495	1200

Table 5.2: Energies of the Doppler shifted γ -rays (E_γ in keV) for ^{58}Ni and ^{112}Sn excitation as a function of relative angle $\phi_{12} = |\phi_\gamma - \phi_p|$ between γ -ray and particle detection. The detection of nickel and tin particles in the PPAC are calculated separately.

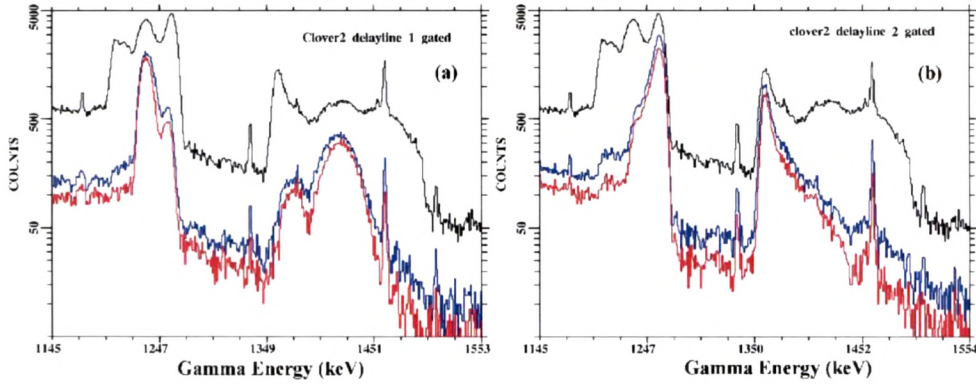


Figure 5.1: Ungated γ -ray spectrum for Clover-2 (black) and γ -ray spectra gated by (a) left delay-line and (b) right delay-line. The spectra in coincidence with the small angle end of the delay line (inner contact readout) are plotted in blue while the spectra in coincidence with the large angle end of the delay line (outer contact readout) are plotted in red. For all spectra the add-back procedure was applied.

This spectrum is compared with two spectra, coloured in blue and red, analysed with a condition that the inner or outer contact of the delay-line registered a particle, respectively. Data are shown for the left half (fig. 5.1a) and right half (fig. 5.1b) of the PPAC. It is clearly seen, that the triple hump structure is only partially reproduced after requiring the additional condition on the delay-line. The γ -ray peaks can only be related to the detection of nickel ions. The slowed-down Sn recoil nuclei could be measured with the φ -segments but not with the delay-line (energy signals are one order of magnitude smaller). For the left delay-line the Sn excitation (fig. 5.1a) should occur at $\sim 1234\text{keV}$ and the Ni excitation at $\sim 1405\text{keV}$ for the detection of target nuclei. When gated on the right delay-line the γ -ray

spectrum of Clover-2 (fig. 5.1b) should show the Sn excitation at 1245-1261keV and the Ni excitation at 1350-1382keV. (for details see Appendix A.3)

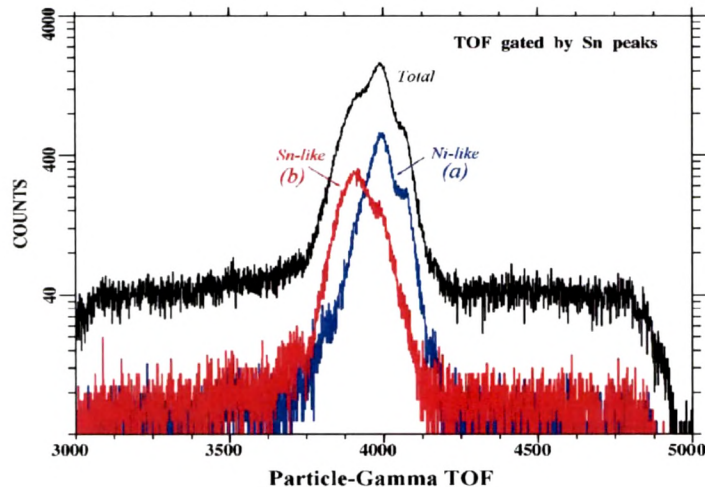


Figure 5.2: Gamma-particle time-of-flight (TOF) spectrum (black) and γ -energy gated spectra for Ni(blue, $E_\gamma=1264\text{keV}$) or Sn(red, $E_\gamma=1200\text{keV}$) particles detected in PPAC.

A time-of-flight (TOF) spectrum was also generated between the γ -ray signal from the Clover detectors and timing from the PPAC detectors. The method of the INGASORT analysis is described in detail in Appendix A.1. The centroids of the time peaks for different φ -segments measured for Ni projectiles were matched within ± 10 channels ($\sim 1\text{ns}$). Fig. 5.2 shows the TOF-spectra for Clover detectors with respect to PPAC detectors gated by different energy windows in the Clover detector. The TOF difference between the scattered projectiles (fig. 5.2a), gated on $E_\gamma=1264\text{keV}$ for Ni detected in PPAC and target recoils ((fig. 5.2b), gated on $E_\gamma=1200\text{keV}$ in Sn detected in PPAC) was found to be too small compared to the timing resolution of the Clover detectors.

5.4 Suppression of the γ -Ray Background Events

As a result of the TOF information, the timing between Clover and PPAC was only sufficient to separate the 'random' events from the 'prompt' coincidences. The events associated with random coincidence between the γ -rays in the Clover detectors and the particles detected in the PPAC were typically less than 1% of the prompt events. Fig. 5.3 shows the γ -spectra for random events (bottom red curve) and the background-subtracted prompt events (top black curve). As expected, the discrete γ -ray transitions due to background radiation (e.g. 1461keV of ^{40}K) disappear in the corrected spectrum.

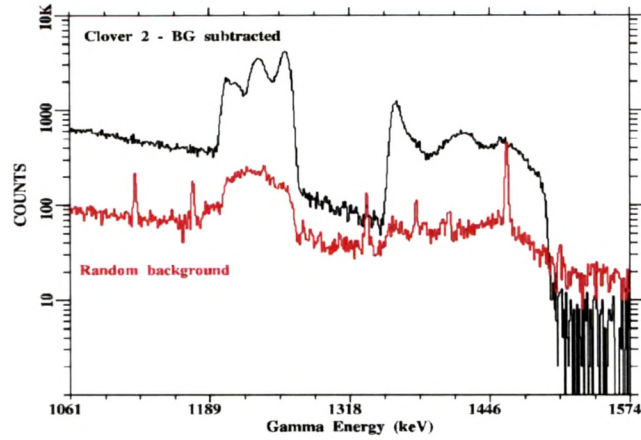


Figure 5.3: γ -spectra associated with the random events (bottom red curve) and background-subtracted prompt spectrum (top black curve).

5.5 Determination of the Scattering Angles

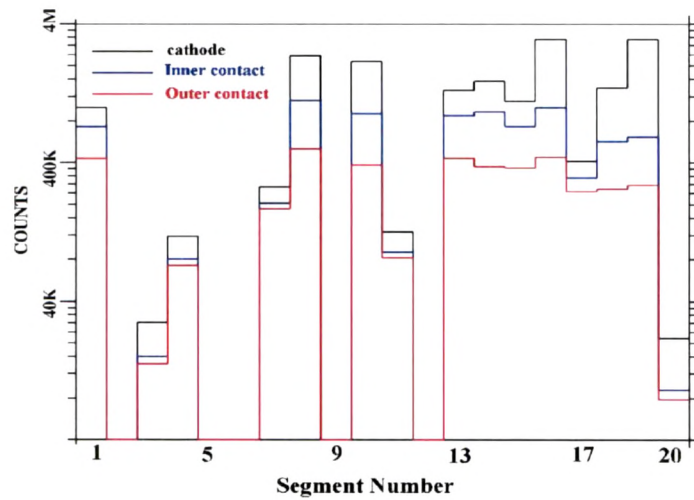


Figure 5.4: Total number of counts recorded for each φ -segment during the γ -p coincidence measurement (black curve). The blue and red histograms show the corresponding counts in coincidence with signals from inner and outer contacts of the delay-lines.

For the angle readout, four signals were recorded from the two ends of the right and left delay-lines. The ϑ information can be obtained by two different methods (**i**) from the

difference in time between the inner and outer contact of the delay-lines ($\text{DDL} = t_{\text{inner}} - t_{\text{outer}}$) and **(ii)** the difference in time between either of the readouts and the timing derived from the anode signals recorded for the individual φ -segments ($\text{SDL} = t_{\text{inner}} - t_{\text{anode}}$). During data collection, some of the φ -segments were completely missing or showed lower count rates compared to the other segments (see fig. 5.4). One also observes different count rates recorded by the inner (blue curve) and the outer contact (red curve) which were a factor of 2-4 lower compared to the raw PPAC signals.

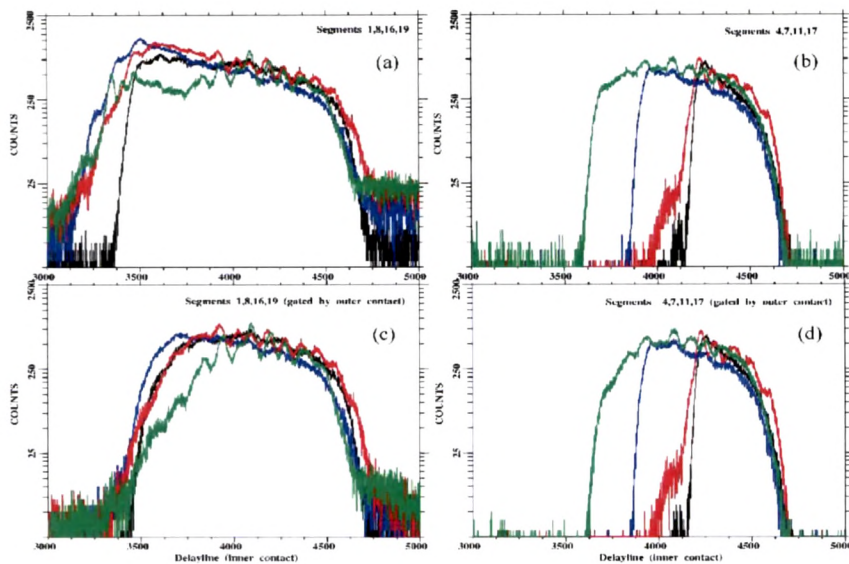


Figure 5.5: Top panel shows the SDL readout for different φ -segments: #1(black), #8(blue), #16(red), #19(green) and #4(black), #7(blue), #11(red) and #17(green). In the bottom panel the corresponding spectra are shown in coincidence with the outer contact.

The SDL readouts for different individual φ -segments are shown in fig. 5.5a-b (top panel). The bottom panel (fig. 5.5c-d) shows the corresponding results gated by a non-zero signal from the outer readout. The following conclusions can be drawn by inspecting these figures. Firstly, the segments having similar count rates in fig. 5.4 show similar delay-line spectra. The edges of these spectra match with the geometrical acceptance angles of 15° - 45° in the laboratory system. Secondly, the φ -segments with a lower counting rate seem to have sometimes a problem with the anode foil at forward angles and consequently show a truncated position spectrum. The difference between top and bottom spectra results from the threshold settings of the constant fractions: particle signals measured at forward angles and attenuated by the delay-line readout are sometimes not registered by the outer contacts. From the observed delay-line spectra, the scattering angle ϑ_p of the Ni projectiles can be calculated from the following relationship

$$\tan\vartheta_p = a \cdot x + b \quad (5.1)$$

where \mathbf{x} is the time difference $t_{inner} - t_{anode}$ and the constants \mathbf{a} and \mathbf{b} are calculated assuming the TAC edges of channels 3400 and 4550 (fig. 5.5) correspond to the angles 15° and 45° , respectively.

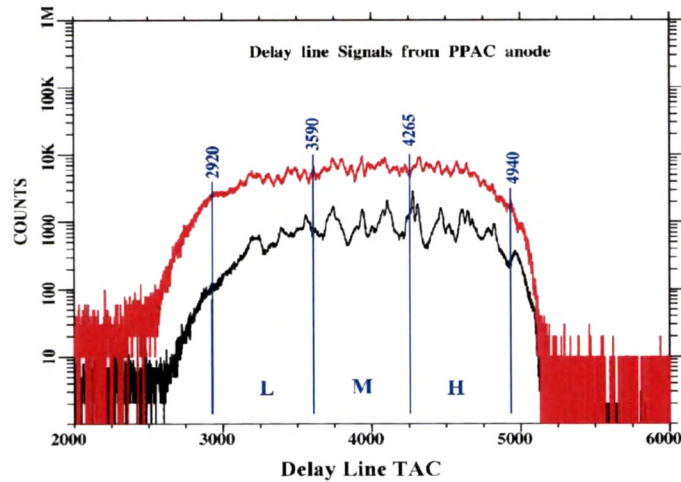


Figure 5.6: DDL spectra for segments 1-10 (black) and segments 11-20 (red). The count rates in both halves are different as there were some of the φ -segments not working during the experiment.

An independent position spectrum (fig. 5.6) was constructed from the time difference spectra between pairs of delay-line signals $DDL = t_{inner} - t_{outer}$. While the right edge of this spectrum corresponds to $\vartheta_p \sim 45^\circ$, the angle corresponding to the left edge is expected to be somewhat larger than the geometrical edge of 15° . From the DDL spectrum, the angle of the detected particle can be calculated by using the similar relationship:

$$\tan\vartheta_p = a \cdot y + b \quad (5.2)$$

where \mathbf{y} is the time difference $t_{inner} - t_{outer}$.

In order to calibrate the DDL spectrum (fig. 5.6), the total angular range was subdivided into three regions L (channels 2920-3590), M (channels 3590-4265) and H (4265-4940). The known SDL spectrum was gated by these three angular regions and the results are shown in fig. 5.7. Using the calibration for the SDL spectrum, the boundaries of the DDL regions corresponds to angles of 21.1° , 28.9° , 36.9° and 43.6° , respectively. With a linear least square fit, the boundaries ($15^\circ, 45^\circ$) of the PPAC are expected at channel 2637 and 5216, respectively.

The azimuthal angle φ_p of the detected particle was calculated from

$$\varphi_p = 18 \cdot [K - \xi] \quad (5.3)$$

where \mathbf{K} is the segment number and ξ is a random number between 0 and 1.

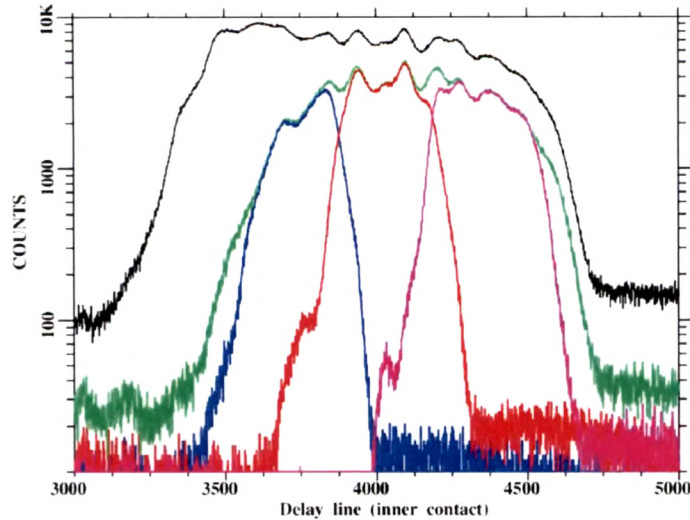


Figure 5.7: SDL spectrum gated by different regions of the DDL spectrum (see fig. 5.6) (i)black -ungated, (ii)green full DDL range, (iii)blue L-region, (iv)red M-region and (v)pink H-region (see text for details)

5.6 Doppler-Shift Correction

From the knowledge of the scattering angles (ϑ_p, φ_p) , the Doppler correction of the measured γ -ray energies can be performed event-by-event. Initially the nominal values $(\vartheta_\gamma, \varphi_\gamma)$ for the centre of the Clover detectors were used for the Doppler correction, but the results were not very satisfying for $E_{\gamma 0}$, showing prominent tailing at both low and higher energy side.

The centroids of the Doppler-corrected peaks showed a residual dependence on the φ -segments. There was also a shift in peak shape between individual crystals (fig. 5.8). Although the peak intensity of the interesting γ -ray transitions was not effected by the peak-shape, systematic errors can be introduced in the estimation of the Compton background under a rather broad peak. It was decided to minimise the peak widths by applying individual Doppler corrections for different Ge crystals instead of a common correction for a Clover detector. Readjustment of calibrations $(\vartheta_\gamma, \varphi_\gamma)$ for individual Ge crystals was carried out to eliminate the residual φ_p dependence.

5.6.1 Method for Improved Doppler Correction

The Doppler-shifted γ -ray energy E_γ is given by

$$E_\gamma \cong E_{\gamma 0} \cdot \left[1 + \frac{v_p}{c} \cdot \cos(\vartheta_{\gamma p}) \right] \quad (5.4)$$

with

$$\cos(\vartheta_{\gamma p}) = \cos(\vartheta_\gamma) \cdot \cos(\vartheta_p) + \sin(\vartheta_\gamma) \cdot \sin(\vartheta_p) \cdot \cos(\varphi_\gamma - \varphi_p) \quad (5.5)$$

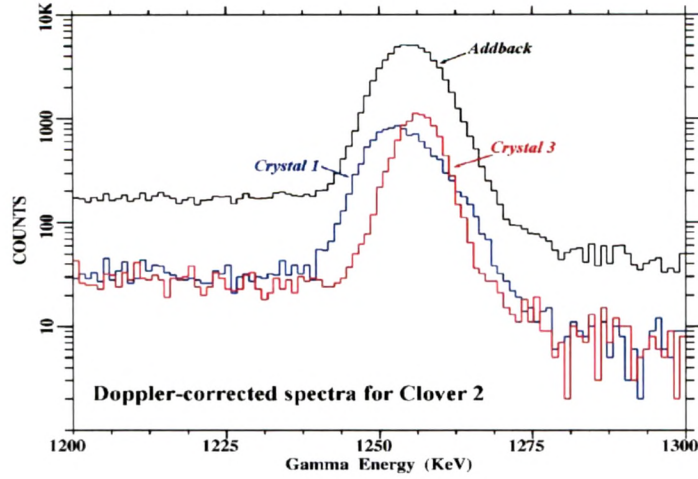


Figure 5.8: Doppler corrected γ -ray spectra for individual crystals of Clover-2 assuming a common correction $(\vartheta_\gamma, \varphi_\gamma)$ for the Clover.

For a given ϑ_p and ϑ_γ , the γ -ray energy shows a strong dependence on the phase angle $\varphi_{\gamma p}$ between both detectors. Since the γ -rays are detected in the backward hemisphere and the scattered projectiles are measured in the forward direction, one obtains $(\vartheta_p + \vartheta_\gamma) \sim 180^\circ$. For the following discussion we define two quantities by

$$E_\gamma^{min} = E_\gamma \cong E_{\gamma 0} \cdot \left[1 + \frac{v_p}{c} \cdot \cos(\vartheta_\gamma + \vartheta_p)\right] \quad (5.6)$$

$$E_\gamma^{max} = E_\gamma \cong E_{\gamma 0} \cdot \left[1 + \frac{v_p}{c} \cdot \cos(\vartheta_\gamma - \vartheta_p)\right] \quad (5.7)$$

The minimum value of γ -ray energy E_γ (for Ni excitation) corresponds to the case $(\varphi_\gamma - \varphi_p) \sim 180^\circ$, when γ -rays and Ni projectiles are detected on diametrically opposite side and it reaches a maximum value when they are detected on the same side $[(\varphi_\gamma - \varphi_p) \sim 0^\circ]$. A plot of E_γ versus φ_p closely resembles a sine-wave (fig. 5.9), given by

$$E_\gamma = A + B \cdot \cos(\varphi_\gamma - \varphi_p) \quad (5.8)$$

From a least-square fit of the experimental energies E_γ with a sine-wave, the quantities E_γ^{min} , E_γ^{max} and φ_γ can be determined. The phase angle φ_γ corresponds to the projectile excitation and $(\pi + \varphi_\gamma)$ to the target excitation.

The calculated variation of E_γ^{max} and E_γ^{min} with the scattering angle ϑ_p for different values of ϑ_γ are shown in fig. 5.10 for Ni excitation (a,b) and Sn excitation (c,d). The angle difference $(\vartheta_\gamma - \vartheta_p)$ can be calculated from E_γ^{max} . The quantity $(\vartheta_\gamma + \vartheta_p)$ determined from E_γ^{min} , is not very well determined since $\cos\vartheta$ is insensitive in the vicinity of $\sim 180^\circ$.

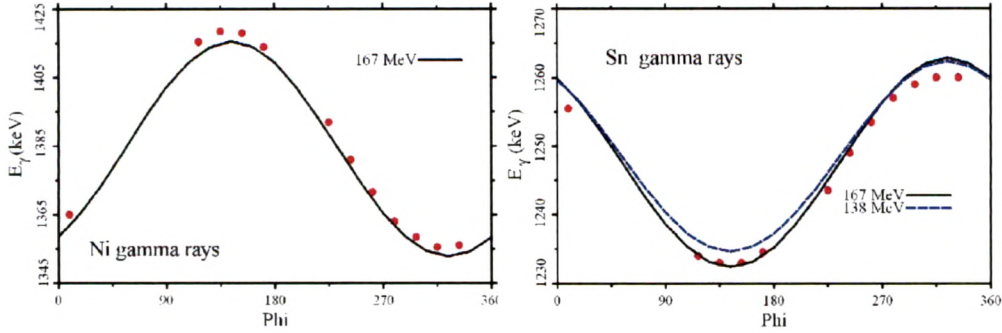


Figure 5.9: Doppler oscillations for Crystal-1 of Clover-2. The circles are experimental centroids for Ni and Sn peaks for gate-M of the DDL spectrum (fig. 5.6). The solid curves correspond to the theoretical predictions for $E_{lab}=167\text{MeV}$, $\vartheta_p = 32.9^\circ$, $\vartheta_\gamma = 142.7^\circ$ and $\varphi_\gamma=143.2^\circ$ (see text). For Sn γ -rays, theoretical curves for two different beam energies $E_{lab}=167\text{MeV}$ and 138MeV are shown. (see also Appendix A.3)

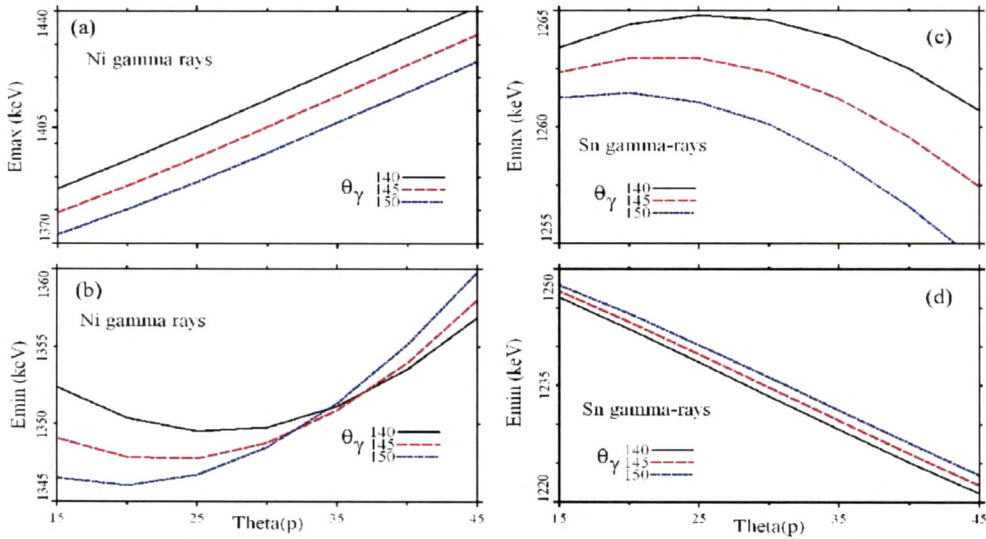


Figure 5.10: Calculated Doppler-shifted peak positions for projectile and target excitation as a function of detector angle ϑ_p . The energy loss in the target was neglected in the above calculations.

We have tried to extract the geometrical angles ($\vartheta_\gamma, \varphi_\gamma$) for the Clover detectors from the experimental data by analyzing the Doppler shift pattern for each Clover crystal as a function of the anode segment φ_p . The DDL position spectrum (fig. 5.6) was divided into three regions

Low (L), Middle (M) and High (H) which nominally corresponded to angular ranges of $\vartheta_p \sim 21.1^\circ$ - 28.9° , 28.9° - 36.9° and 36.9° - 43.6° . For each combination, the γ -ray spectra from a given Ge-crystal gated by different φ -segments ($3 \times 4 \times 4 \times 20$ spectra) were collected and the peak centroids for the projectile and target excitation γ -rays were determined. The geometrical angles ($\vartheta_\gamma, \varphi_\gamma$) for each Clover crystal were adjusted to reproduce the phase and amplitude of oscillation for the Ni excitation. Since the lifetime of the 2^+ states in Ni and Sn are larger than the transit times through the target foil, the γ -decay takes place primarily after passing the target. Therefore, an effective beam energy of $E_{lab} = 167$ MeV (~ 8 MeV energy loss in the target) was used for the Doppler correction of the Ni excitation. The extracted average ($\vartheta_\gamma, \varphi_\gamma$) for each crystal are summarised in Tab. 5.3.

CLOVER #	Crystal-1		Crystal-2		Crystal-3		Crystal-4	
	$\vartheta_\gamma [^\circ]$	$\varphi_\gamma [^\circ]$						
1	130.7	53.4	140.3	64.9	146.1	55.5	140.5	43.5
2	142.7	144.2	147.6	124.4	137.0	118.9	133.2	132.9
3	137.1	-33.4	143.8	-46.9	135.3	-56.5	128.8	-44.0
4	144.5	-114.1	138.9	-129.2	128.3	-118.0	135.4	-106.5

Table 5.3: Gamma-ray detection angles ($\vartheta_\gamma, \varphi_\gamma$) for each Ge-crystal extracted from the Doppler shift data of the Ni excitation (effective beam energy $E_{lab} = 167$ MeV).

For γ -rays of Sn excitation, shown in the right panel of fig. 5.9, the calculated amplitude of the Doppler oscillations are overestimated by about 10% using the values ($\vartheta_\gamma, \varphi_\gamma$) needed to reproduce the γ -rays for Ni excitation. This difference can be qualitatively understood by incorporating the significant energy loss of the slow moving Sn recoils. The program SHRIM-2008 [37] was used to calculate the specific energy loss of Ni and Sn nuclei in the Sn target. For a target thickness of ~ 0.55 mg/cm² one calculates an average energy loss of the Sn recoils, which is $\sim 20\%$ of the initial value. In the Doppler correction routine of the INGASORT analysis, the required recoil velocity (10% reduction) was simulated by reducing the effective beam energy by 20% to $E_{lab} = 138$ MeV (Appendix A.4).

For single-hit γ -events, the angles ($\vartheta_\gamma, \varphi_\gamma$) for individual Ge-crystals were used. For multi-hit γ -events, we used the average angle of the involved Ge-crystals. This is a reasonable assumption as computer simulation indicates that double-hit events (which correspond to about 50% of single-hit events) are localised near the common edge of the Ge-crystals.

Fig. 5.11 shows the final Doppler-corrected γ -ray spectra for the systems $^{112}\text{Sn} + ^{58}\text{Ni}$ and $^{116}\text{Sn} + ^{58}\text{Ni}$ for target (top) and projectile excitation (middle). For completeness the uncorrected γ -ray spectra are shown at the bottom.

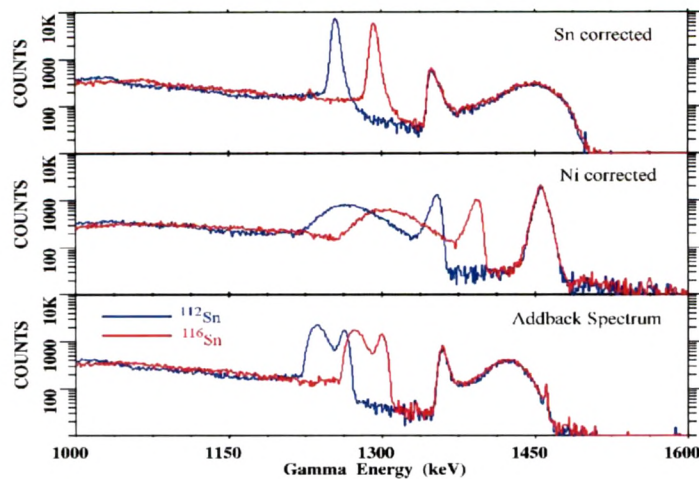


Figure 5.11: Doppler corrected γ -ray spectra for the systems $^{112}\text{Sn}+^{58}\text{Ni}$ (blue) and $^{116}\text{Sn}+^{58}\text{Ni}$ (red). The uncorrected spectra are shown at the bottom.

5.7 Experimental γ -Ray Yields

The Doppler-corrected add-back spectra for Coulomb excitation of Ni and Sn are shown in fig. 5.12. For comparison, the 'random' background is also shown. One observes a rather smooth distribution with a residual peaking of less than 1% relative to the 'prompt' peak area. Therefore, a linear background underneath the 'prompt' peak was assumed. For extracting the γ -ray yields, the peak shape was assumed to be Gaussian in nature with exponential tail on both sides. To reduce systematic errors, identical line shapes were used to extract peak areas for ^{112}Sn excitation (1257keV) and ^{116}Sn excitation (1294keV).

We used two different methods for the determination of the particle angular range: (i) DDL readout which yield a reduced γ -ray background but was limited in angular acceptance range $\vartheta_p \sim 21^\circ$ - 44° and (ii) SDL readout having a larger acceptance range of $\vartheta_p \sim 15^\circ$ - 44° but suffered from increased γ -ray background due to higher 'random' events. The experimental γ -ray yields for projectile and target excitation and the $^{112}\text{Sn}/^{116}\text{Sn}$ γ -ray ratios, extracted using DDL and SDL readouts are tabulated in tab. 5.4 and tab. 5.5, respectively. For Clover-1 and Clover-4, one of the crystals (#2) showed considerable gain drift during the experimental run and has been excluded from the analysis. Crystal-4 of Clover-4 had a much poorer intrinsic resolution ($\sim 10\text{keV}$) compared to the other three (2.53keV) and was also been excluded. As a result, the absolute number of counts from Clover-1 and Clover-4 were substantially smaller than those of Clover-2 and Clover-3.

Both methods gave very similar results despite covering different angular ranges. The insensitive dependence of $^{112}\text{Sn}/^{116}\text{Sn}$ ratio on the angular range will be discussed later in the context of the Coulomb excitation calculations.

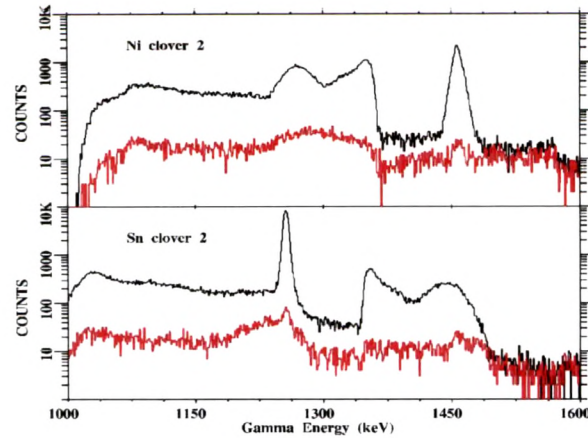


Figure 5.12: Doppler corrected add-back spectra for Clover-2. The black and red curves correspond to spectra under 'prompt' and 'random' conditions in Clover-PPAC TOF spectrum. The top and bottom spectra correspond to Doppler corrections assuming projectile (Ni) excitation and target (Sn) excitation.

Clover #	^{112}Sn target		^{116}Sn target		$^{112}\text{Sn}/\text{Ni}$	$^{116}\text{Sn}/\text{Ni}$	$^{112}\text{Sn}/^{116}\text{Sn}$
	Sn exc	Ni exc	Sn exc	Ni exc	ratio	ratio	ratio
1	26237 ± 233	11142 ± 155	21208 ± 224	12129 ± 173	2.355 ± 0.039	1.748 ± 0.031	1.346 ± 0.032
2	59050 ± 349	25093 ± 275	48567 ± 393	27902 ± 297	2.353 ± 0.029	1.741 ± 0.023	1.352 ± 0.025
3	55357 ± 378	23732 ± 247	44573 ± 303	25656 ± 283	2.333 ± 0.030	1.737 ± 0.022	1.343 ± 0.024
4	19488 ± 202	8160 ± 129	15614 ± 180	9124 ± 138	2.388 ± 0.045	1.711 ± 0.032	1.396 ± 0.0037

Table 5.4: Peak areas and intensity ratios for Sn and Ni excitation (exc) in $^{112}\text{Sn}+^{58}\text{Ni}$ and $^{116}\text{Sn}+^{58}\text{Ni}$ systems using the DDL analysis.

5.7.1 Dependence of $^{112}\text{Sn}/^{116}\text{Sn}$ Ratio on the Azimuthal Angle

It was already shown that the γ -ray energy resolution for different φ -segments depends strongly on the relative phase difference $\varphi_{\gamma p} = (\varphi_{\gamma} - \varphi_p)$ ($|dE_{\gamma}/d\varphi|$ is minimum for $\varphi_{\gamma p} \sim 0^{\circ}$ and $\sim 180^{\circ}$). The particle- γ angular correlations for Ni and Sn nuclei are also expected to be significantly different in the laboratory frame.

In order to check the sensitivity of the $^{112}\text{Sn}/^{116}\text{Sn}$ ratio to this dependence, we have subdivided the data into two halves of the PPAC: (i) $|\varphi_{\gamma} - \varphi_p| < 90^{\circ}$ and (ii) $90^{\circ} < (\varphi_{\gamma} - \varphi_p) < 270^{\circ}$. The resulting spectra are shown in fig. 5.13 for Clover-2. The areas under the Sn and Ni peaks are tabulated in tab. 5.6. Although the Sn/Ni ratios were sensitive to the φ -range selected in this analysis, the overall ratio for $^{112}\text{Sn}/^{116}\text{Sn}$ was not

Clover #	¹¹² Sn target		¹¹⁶ Sn target		¹¹² Sn/Ni	¹¹⁶ Sn/Ni	¹¹² Sn/ ¹¹⁶ Sn
	Sn exc	Ni exc	Sn exc	Ni exc	ratio	ratio	ratio
1	30932±251	12969±204	24496±251	13823±219	2.385±0.043	1.772±0.033	1.345±0.035
2	69957±416	28984±330	56421±456	31659±344	2.413±0.031	1.782±0.024	1.354±0.025
3	65376±532	27426±363	51903±504	29202±389	2.383±0.037	1.777±0.029	1.341±0.030
4	24042±240	10025±154	19005±230	10928±161	2.398±0.043	1.739±0.033	1.379±0.0036

Table 5.5: Peak areas and intensity ratios for Sn and Ni excitation (exc) in ¹¹²Sn+⁵⁸Ni and ¹¹⁶Sn+⁵⁸Ni systems using the SDL analysis.

varying at all.

$\varphi_{\gamma p}$	¹¹² Sn target		¹¹⁶ Sn target		¹¹² Sn/Ni	¹¹⁶ Sn/Ni	¹¹² Sn/ ¹¹⁶ Sn
	Sn exc	Ni exc	Sn exc	Ni exc	ratio	ratio	ratio
-90°-90°	24993±158	10799±208	21040±314	12194±295	2.314±0.046	1.725±0.049	1.341±0.046
90°-270°	33800±343	14069±438	27597±260	15377±553	2.402±0.078	1.794±0.066	1.338±0.066

Table 5.6: φ -dependence of particle- γ intensities (Clover-2)

5.8 Experimental ¹¹²Sn/¹¹⁶Sn Intensity Ratio

From the weighted average of four measurements (using four Clover detectors) the intensity ratio ¹¹²Sn/¹¹⁶Sn is given by

$$\begin{aligned}\sigma(^{112}\text{Sn})/\sigma(^{116}\text{Sn}) &= 1.347 \pm 0.015 \text{ (DDL analysis)} \\ \sigma(^{112}\text{Sn})/\sigma(^{116}\text{Sn}) &= 1.348 \pm 0.017 \text{ (SDL analysis)}\end{aligned}$$

5.8.1 Correction for Photopeak Efficiency

The measured ¹¹²Sn/¹¹⁶Sn intensity ratio had to be corrected for the photopeak efficiency of the different Doppler shifted γ -ray energies E_γ . A ¹⁵²Eu source placed at the target position was used for relative efficiency determination. In the limited energy range 1.0-1.5MeV, the efficiency curve could be approximated by an exponential function given by

$$f(E) \sim f_0 \cdot \exp(-E/E_0) \quad (5.9)$$

with $E_0 \approx 2096, 2184, 2245$ and 2262keV for Clover-1 to Clover-4, respectively. Since the difference in the energies of the Doppler shifted peak is small, the ratio of the two efficiencies can be approximated as:

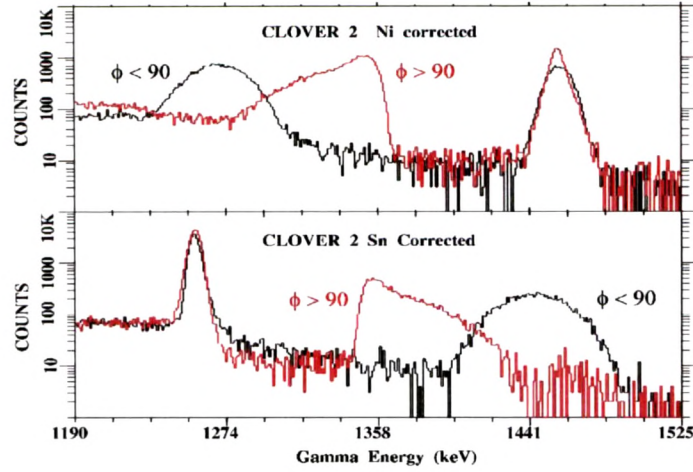


Figure 5.13: Doppler corrected add-back spectra for Clover-2. The black and red spectra correspond to correlations for $-90^\circ < \varphi_{\gamma p} < 90^\circ$ and $90^\circ < \varphi_{\gamma p} < 270^\circ$. The top and bottom sets correspond to Doppler corrections assuming projectile and target excitations.

$$f(^{112}\text{Sn})/f(^{116}\text{Sn}) \approx \exp(\Delta E/E_0) \approx 1.017 \pm 0.001$$

$\Delta E \approx (1293.5 - 1256.8) \cdot (1249.0 / 1256.8) = 36.5 \text{ keV}$ is the shifted energy difference between the two γ -ray transitions. The double ratio, **corrected for the detector efficiency**, is given by

$$\sigma(^{112}\text{Sn})/\sigma(^{116}\text{Sn}) = 1.324 \pm 0.015$$

5.8.2 Correction for Isotopic Impurity

The used Sn targets were enriched to $99.5\pm 0.2\%$ and $98.0\pm 0.1\%$ for ^{112}Sn and ^{116}Sn , respectively. For the Ni excitation, all Sn isotopes contribute equally. On the other hand, the excitation of the different Sn isotopes can be discriminated due to their different transition energies (see table below).

Isotope	^{112}Sn	^{114}Sn	^{116}Sn	^{118}Sn	^{120}Sn
2^+ energy (keV)	1257	1300	1293	1230	1171

Except for the pair $^{114,116}\text{Sn}$, other γ -rays can be uniquely identified (energy resolution $\sim 6\text{keV}$ after Doppler correction). The amount of ^{114}Sn impurity in the ^{116}Sn target is reported to be less than 0.1%. The measured $^{112}\text{Sn}/^{116}\text{Sn}$ intensity ratio should therefore be reduced by a factor corresponding to the isotopic purity of the targets:

$$(98.0\pm 0.1\%)/(99.5\pm 0.2\%) = 0.985\pm 0.003$$

The **final double ratio**, corrected for detector efficiency and target purity, is given by

$$\sigma(^{112}\text{Sn})/\sigma(^{116}\text{Sn})=1.305\pm 0.015$$

5.8.3 Coulomb Excitation Cross Sections

Coulomb excitation calculations were performed with the Winther-de Boer Coulex code [38]. In a first step the excitation cross sections were calculated as a function of the reduced transition matrix elements (see Appendix A.5 and A.7). Since, the time scales for the excitation ($\sim 10^{-22}\text{s}$) and decay (10^{-15} - 10^{-9}s) are quite different, the γ -decay was determined with a separate computer code (see Appendix A.6). For the particle- γ angular correlation we can distinguish three cases: (i) calculation in the rest-frame (input parameter I24=1, $Q_0=1$, $Q_2=0$, $Q_4=0$), (ii) calculation in the laboratory frame (only Lorentz-boost, input parameter I24=0, $Q_0=1$, $Q_2=0$, $Q_4=0$), (iii) calculation in the laboratory frame with γ -ray angular correlation (input parameter I24=0, $Q_0=Q_2=Q_4=1$). In table. 5.7 the cross sections for the $^{58}\text{Ni}\rightarrow^{116}\text{Sn}$ system at 175MeV are given for two different angular ranges in the laboratory frame: $\vartheta_{lab}=15^\circ$ - 45° and $\vartheta_{lab}=21.1^\circ$ - 43.7° . For the excitation of ^{116}Sn a $B(E2;0^+\rightarrow 2^+)=0.209e^2b^2$ value was used (see Appendix A.2).

In a second step the cross sections were calculated for $^{58}\text{Ni}\rightarrow^{112}\text{Sn}$ system at 175MeV for the same angular ranges: $\vartheta_{lab}=15^\circ$ - 45° and $\vartheta_{lab}=21.1^\circ$ - 43.7° and the results are given in table. 5.8. For the excitation of ^{112}Sn a $B(E2;0^+\rightarrow 2^+)=0.240e^2b^2$ value was used (Appendix A.2).

From both tables the double ratio $^{112}\text{Sn}/^{116}\text{Sn}$ was determined (see the table. 5.9) A comparison of these effects shows that the analysis is completely insensitive to the γ -ray angular distribution and the different angular ranges. Since the g-factor of the first excited state in all Sn isotopes is very small ($g(2^+)\sim 0$), one expects no distortion of the γ -ray angular distribution due to the deorientation effect. Therefore, the calculated double ratio 1.283 for the angular range of $\vartheta_{lab}=21.1^\circ$ - 43.7° was used to determine from the experimental double ratio 1.305 ± 0.024 the $B(E2)$ -value for ^{112}Sn using the following formula:

$\vartheta_\gamma\varphi_\gamma$	θ_{cm}		$^{116}\text{Sn}:\sigma_2[\text{mb}]$	$^{58}\text{Ni}:\sigma_2[\text{mb}]$	ratio
			$^{58}\text{Ni}\rightarrow^{116}\text{Sn}$	$^{58}\text{Ni}\rightarrow^{116}\text{Sn}$	$^{116}\text{Sn}/^{58}\text{Ni}$
			175MeV	175MeV	
135°,55°	22.4°-65.7°	(i)	60.80	39.77	1.529
		(ii)	59.94	36.46	1.644
		(iii)	61.63	38.26	1.611
	31.5°-63.9°	(i)	53.09	35.07	1.514
		(ii)	52.34	32.14	1.629
		(iii)	53.80	33.72	1.596

Table 5.7: Cross sections for the $^{58}\text{Ni}+^{116}\text{Sn}$ system at 175MeV for two different angular ranges.

$\vartheta_\gamma\varphi_\gamma$	θ_{cm}		$^{112}\text{Sn}:\sigma_2[\text{mb}]$	$^{58}\text{Ni}:\sigma_2[\text{mb}]$	ratio
			$^{58}\text{Ni}\rightarrow^{112}\text{Sn}$	$^{58}\text{Ni}\rightarrow^{112}\text{Sn}$	$^{112}\text{Sn}/^{58}\text{Ni}$
			175MeV	175MeV	
135°,55°	22.7°-66.5°	(i)	74.88	37.98	1.972
		(ii)	73.78	34.81	2.120
		(iii)	75.78	36.52	2.075
	31.8°-64.7°	(i)	65.32	33.63	1.942
		(ii)	64.37	30.75	2.093
		(iii)	66.05	32.26	2.046

Table 5.8: Cross sections for the $^{58}\text{Ni}+^{112}\text{Sn}$ system at 175MeV for two different angular ranges.

$\vartheta_\gamma\varphi_\gamma$	ϑ_{lab}		ratio
			$^{112}\text{Sn}/^{116}\text{Sn}$
135°,55°	15°-45°	(i)	1.290
		(ii)	1.290
		(iii)	1.288
	21.1°-43.7°	(i)	1.283
		(ii)	1.285
		(iii)	1.283

Table 5.9: Double ratio of $^{112}\text{Sn}/^{116}\text{Sn}$ as determined from tab. 5.7 and tab. 5.8

$$B(E2;0^+ \rightarrow 2^+) = \frac{1.305}{1.283} \cdot 0.240e^2b^2 = 0.244e^2b^2$$

Since the $B(E2)$ values are directly proportional to the Coulomb excitation cross sections, the error of the $B(E2)$ -value for ^{112}Sn was determined from the $B(E2)$ ratio

$$\frac{B(E2; 0^+ \rightarrow 2^+)_{112-\text{Sn}}}{B(E2; 0^+ \rightarrow 2^+)_{116-\text{Sn}}} = \frac{B(E2; 0^+ \rightarrow 2^+)_{112-\text{Sn}}}{0.209(6)} = 1.168(22) \quad (5.10)$$

The error propagation ($df^2 = (x \cdot dy)^2 + (y \cdot dx)^2$) for a product ($f = x \cdot y$) yields the following result

$$B(E2;0^+ \rightarrow 2^+) = 0.244(8) e^2b^2$$

Additional Coulomb excitation calculations were performed taking into account the slowing-down of the projectiles in the targets. A corrected beam energy of 171MeV was used in order to consider the slowing down in 50% of the target thickness. For ^{58}Ni projectiles at 175MeV slowed down in a Sn target (0.53 mg/cm^2) an energy loss of $\frac{dE}{dx} = 16.4 [\frac{\text{MeV}}{\text{mg/cm}^2}]$ was calculated. The slowing down of the projectiles changed the calculated double ratio by less than 0.8%.

Calculations included the feeding contributions from the 0_2^+ , 2_2^+ , 3_1^- and 4_1^+ states in ^{112}Sn and ^{116}Sn , which were obtained from the known excitation strengths given in Appendix A.2. In both cases the summed intensity from decays of higher-lying states added up to less than 2% of the $2_1^+ \rightarrow 0_{g.s.}^+$ decay intensity, which agreed with our experimental findings. The calculated double ratio changed by less than 1% when the feeding states were neglected.

The final $B(E2)$ value for ^{112}Sn , which includes the slowing down of ^{58}Ni projectiles in the Sn targets and the feeding contributions from higher lying states is given in tab. 5.10 together with the extracted $B(E2)$ value for ^{114}Sn measured at GSI.

Isotope	$B(E2;0^+ \rightarrow 2^+)$
^{112}Sn	$0.242(8)e^2b^2$
^{114}Sn	$0.232(8)e^2b^2$

Table 5.10: Measured reduced transition probabilities for ^{112}Sn and ^{114}Sn .